

Article

Double-Tuned Birdcage Radio Frequency Coil for 7 T MRI: Optimization, Construction and Workbench Validation

Alessandra Retico ¹, Francesca Maggiorelli ^{1,2,3}, Giulio Giovannetti ⁴, Eddy Boskamp ⁵, Fraser Robb ⁶, Marco Fantasia ⁷, Angelo Galante ^{7,8,9,*}, Marcello Alecci ^{7,8,9}, Gianluigi Tiberi ^{10,11} and Michela Tosetti ^{3,12}

¹ Pisa Division, National Institute for Nuclear Physics (INFN), 56127 Pisa, Italy

² Department of Physical Sciences, Earth and Environment (DSFTA), University of Siena, 53100 Siena, Italy

³ Imago7 Foundation, 56128 Pisa, Italy

⁴ Institute of Clinical Physiology, National Research Council (CNR), 56124 Pisa, Italy

⁵ Hyperfine Research Inc., Guilford, CT 06437, USA

⁶ GE Healthcare Inc., Aurora, OH 44202, USA

⁷ Department of Life, Health & Environmental Sciences (MESVA), University of L'Aquila, 67100 L'Aquila, Italy

⁸ Gran Sasso National Laboratory, INFN, 67100 L'Aquila, Italy

⁹ SPIN-CNR, c/o Department of Physical and Chemical Science, University of L'Aquila, 67100 L'Aquila, Italy

¹⁰ School of Engineering, London South Bank University, London SE1 0AA, UK

¹¹ Umbria Bioengineering Technologies (UBT) Srl, 06081 Perugia, Italy

¹² IRCCS Stella Maris Foundation, 56128 Pisa, Italy

* Correspondence: angelo.galante@univaq.it

Abstract: The aim of the present study is the optimization, construction, and workbench validation of a double-tuned ¹H- ²³Na volume radio frequency (RF) coil suitable for human head imaging at 7 T, based on the birdcage geometry. The birdcage-like design which is considered is the four-ring model, in which two standard birdcage-like structures with the same diameters are nested along the longitudinal axis. Simulations based on Maxwell's equations are performed to evaluate the RF magnetic field homogeneity and the RF coil efficiency varying the coil geometrical parameters. The RF magnetic field homogeneity is evaluated both on the transverse ($z = 0$) and longitudinal ($y = 0$) planes without performing the impedance matching procedure, so that the RF coil symmetry is not perturbed by the matching network. The RF coil efficiency is instead dependent on the effective coil input RF power, and it is evaluated after matching the coil, so that the reflected power is minimized, assuming that the stimulation power is totally delivered to the RF coil. Considering the simulation results and the target application, the useful RF coil geometrical parameters are fixed. The four-ring model, which showed the best performances, has been built and tested on a workbench, using a cylindrical phantom filled with a 0.05 M saline solution as load. This provides the first example of a four-ring realization intended ¹H- ²³Na for human head imaging at 7 T.

Keywords: UHF MRI; 7 T MRI; RF coils; double tuned; sodium imaging



Citation: Retico, A.; Maggiorelli, F.; Giovannetti, G.; Boskamp, E.; Robb, F.; Fantasia, M.; Galante, A.; Alecci, M.; Tiberi, G.; Tosetti, M.

Double-Tuned Birdcage Radio Frequency Coil for 7 T MRI: Optimization, Construction and Workbench Validation. *Electronics* **2023**, *12*, 901. <https://doi.org/10.3390/electronics12040901>

Academic Editor: Yalin Zheng

Received: 21 December 2022

Revised: 25 January 2023

Accepted: 1 February 2023

Published: 10 February 2023



Copyright: © 2023 by the authors. Licensee MDPI, Basel, Switzerland. This article is an open access article distributed under the terms and conditions of the Creative Commons Attribution (CC BY) license (<https://creativecommons.org/licenses/by/4.0/>).

1. Introduction

After its introduction in 1985 by Hayes [1], birdcage geometry has become the most extensively studied and discussed RF coil for low field and high field MRI. Its structure consists of conductive paths, called legs and end-rings. In the standard design, the legs, arranged on a cylindrical surface and equally spaced to each other, are connected through a pair of so-called end-rings. When the birdcage RF coil is excited, 'waves' propagate along the periodic structure and for some frequencies they combine constructively and create stationary states, corresponding to the resonant modes. The circuitual model of the birdcage coil is a ladder network of elementary meshes. Each mesh can be described as a two-port L network, corresponding to each physical mesh of the RF coil [2]. The coil is tuned at the working frequency by inserting capacitors along the conductive paths. Depending on the position of the tuning capacitors, a birdcage coil can be implemented in two different

designs, called Low-Pass (LP) or High-Pass (HP). The spectral distribution of the birdcage coil resonant modes depends on the chosen design (LP or HP) and on the number of legs, and it can be derived in a relatively simple way by the circuit model [2,3]. Elegant analytic descriptions of the birdcage resonant modes, including explicit formulation of all mutual interaction between adjacent meshes, can be found in the literature [4].

More recently, birdcage RF coils have been successfully used in the field of X-nuclei MRI, where the signal of a first nucleus (^1H) and a second nucleus (e.g., ^{13}C , ^{23}Na , ^{31}P , etc.) need to be detected with high signal-to-noise-ratio (SNR) and excellent spatial homogeneity. There has always been significant interest to investigate structural MRI together with signals from non-proton nuclei, either MRI or MRS. However, most applications were constrained by limited SNR. With the growing availability of 7 T MR scanners, there is new hope that valuable information from nuclei with low concentrations and low gyromagnetic ratios can be used as new biomarkers in a variety of diseases, ranging from neurodevelopmental disorders to those of the elderly population. Sodium ^{23}Na can provide important information for diagnostic and prognostic evaluations, in pathological processes with suspected links to sodium ion channels, with change in sodium compartmentalization (e.g., shift from extra- to intra-cellular), and/or with sodium accumulation within the tissue. The increasing amount of complementary information (anatomical, metabolic and from different nuclei) accessible by MRI and MRS, can become a major driver of personalized medicine using 7 T equipment.

A range of designs have already been explored to implement double-tuned (DT) volume RF coils, including the recent configuration of nested birdcage RF coils [5,6]. Basically, the following three designs have been proposed. The first involves an LP birdcage in which the legs are alternatively tuned to the two working frequencies, adding a shunt LC network (trap circuit) in series to the Low-Frequency (LF) tuning capacitor tuned at the High-Frequency (HF) [7–10].

The second design, called nested in the following, involves two concentric and independent birdcages with different diameters placed one inside another [11–13]. The outer birdcage is usually longer than the inner one, so that the coupling between the inner and outer birdcage end-rings is minimized. Furthermore, the coupling between the two structures can be minimized by rotating the outer coil with respect to the inner one of a proper angle [6].

The third design, called the four-ring (4R) model, consists of three resonant structures [14,15]. The inner structure is a standard LP birdcage usually tuned at the low frequency, corresponding to X nucleus rather than ^1H [16] and its efficiency is like that of an equivalent single-tuned birdcage coil [17]. The two outer structures are nested on the inner one sharing the legs and one end-ring with the internal LP birdcage. They are usually tuned at high frequency, and they can be designed as HP or LP birdcage-like configurations, depending on the position of the tuning capacitors. If the tuning capacitors are inserted in the external segments of the shared legs, the LP–LP configuration is achieved. Otherwise, when the tuning capacitors are inserted in the two outer end-rings, the LP–HP configuration is achieved [18]. The LP–HP configuration is usually chosen when the ratio between the two working frequencies is relatively large (>2), as in the case of proton–sodium DT-RF coils [14]. In general, obtaining the maximal SNR requires an optimised inner and outer leg length ratio, which can cause a remarkable increase in overall coil length [14]. However, an excessive distance between outer end-rings can restrict the accessible space, which could limit its application for in vivo brain studies performed with small coils. When the RF coil length increases, its use becomes impractical, then different 4R designs can be employed, characterized by short [19] and folded [15] configurations or based on different coil structures [20]. In addition to those described, a further RF coil structure based on the birdcage was constituted by a “modified” DT $^1\text{H}/^{31}\text{P}$ birdcage for simultaneous imaging and spectroscopy studies of the head at 7 T, where the capacitors in the end-rings were removed and other capacitive branches were positioned between the leg extremities and the

shield. Such configuration provided additional transverse electromagnetic modes (TEM) to the birdcage spectrum [21].

Sodium MRI applications are vast and diverse for both preclinical and clinical applications [22–37]. However, the current study has been focalized on the sodium MRI of the human head at ultra-high-field (UHF) (>3 T). Since sodium nuclei have lower concentration than hydrogen in the human body and lower gyromagnetic ratio, the relevance in using UHF MRI is mainly related to its capability of enhancing the SNR.

The goal of the current work is the optimization and construction of a proton–sodium DT birdcage RF coil prototype for 7 T human head MRI. To this purpose, the 4R birdcage model was designed and characterized through electromagnetic simulations. In a first stage, the B_1^+ field homogeneity and the RF coil efficiency of the 4R model were optimized with respect to the coil geometrical parameters through electromagnetic simulations. In a second stage, the geometrical parameters of the 4R DT-RF coil model, which showed the best performances, were fixed and a 7 T RF coil prototype was designed, built, and tested on the workbench.

2. Materials and Methods

The 7 T DT-RF birdcage coil model described in the following is designed to be driven in quadrature at both frequencies (^1H , 298 MHz; ^{23}Na , 79 MHz). This choice is motivated by the fact that a birdcage coil driven in quadrature mode produces a circularly polarized magnetic field with an improvement in the effective B_1^+ field amplitude of a $\sqrt{2}$ factor [38].

In the design optimization, two parameters were considered: the magnetic field homogeneity and the RF coil efficiency. Both parameters were evaluated through electromagnetic simulations (CST Microwave Studio, <http://www.cst.com>, accessed on 15 December 2022) [39]. Figure 1 shows the surface current distributions for both frequencies. We notice that the lower ^{23}Na and higher ^1H modes are provided, respectively, by the longer and shorter rings.

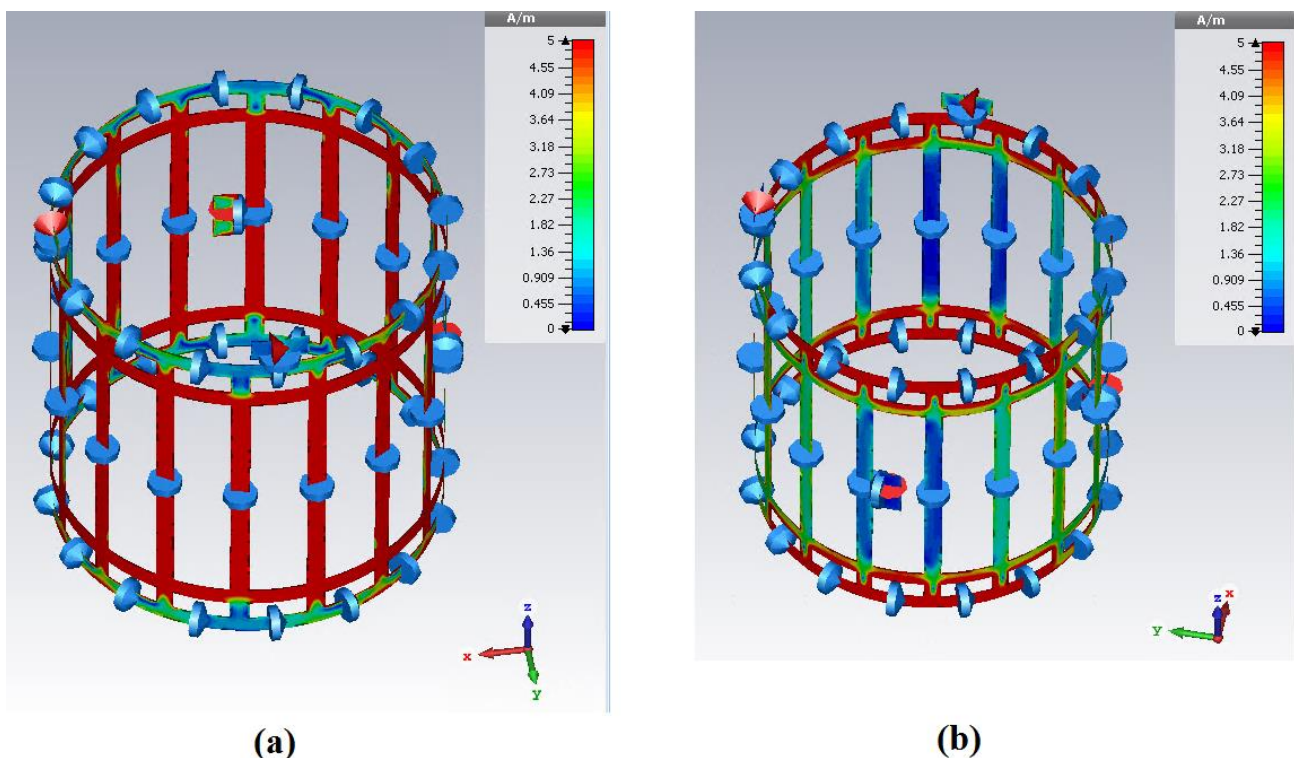


Figure 1. Surface current distribution (A/m) of the 7 T four-ring DT-RF birdcage coil model at the sodium (78.86 MHz) (a), and proton (298.03 MHz) (b), Larmor frequencies.

First, the B_1^+ field homogeneity and the DT-RF coil efficiency of the 4R birdcage model were evaluated by varying the geometrical parameters. The 4R RF coil internal diameter and lengths were fixed considering the final target application, which is an MRI of the human head.

The complex magnetic field $B(x,y,z)$ in a sub-volume of the computational space can be obtained through electromagnetic simulations [39]. We are interested in extracting the circularly polarized component of the transverse magnetic field, $B_1^+(x,y,z)$, which generates the MRI signal. Thus, two slices, corresponding to the central transverse plane ($z = 0$) and longitudinal plane ($y = 0$) were chosen, and the transverse $B_1^+(x,y)$ and longitudinal $B_1^+(x,z)$ fields were calculated from:

$$B_1^+ = [Re\{B_x(x,y,z)\} + j Im\{B_x(x,y,z)\}] + j[Re\{B_y(x,y,z)\} + j Im\{Re\{B_y(x,y,z)\}\}] \quad (1)$$

Once the field maps were obtained, the RF homogeneity on the transverse (xy) and longitudinal (xz) planes were evaluated as [34]:

$$RF \text{ field homogeneity} = \left[1 - \frac{\max(|B_1^+|) - \min(|B_1^+|)}{\max(|B_1^+|) + \min(|B_1^+|)} \right] \quad (2)$$

To better understand the DT-RF coil behavior, the transverse and longitudinal profiles were extracted from the $B_1^+(x,y)$ and $B_1^+(x,z)$ field maps, respectively.

At this stage, the matching procedure was not performed. Indeed, the matching network introduces geometrical asymmetries which cause an increase in the RF field inhomogeneity related to the matching network itself and not to the RF coil geometry. Anyway, in practical conditions the asymmetry introduced by the matching network can be restored following the procedure described in [40].

The second optimization parameter considered was the RF coil efficiency, which depends on the effective input power coupled to the RF coil [5]:

$$RF \text{ field } Eff = \frac{average(|B_1^+|)/\max(|B_1^+|)}{\sqrt{P_{input}}} \quad (3)$$

The matching procedure was performed to guarantee that the reflected power at each input port was minimized and negligible (less than -12 dB), to make reasonable the statement that the transmit power is totally delivered to the RF coil.

After evaluation of the two optimization parameters for a total of six different geometric models in unloaded and loaded (with a spherical phantom, mimicking the human head dimension: diameter 180 mm; $\epsilon_r = 80$, $\sigma = 0.6$ S/m to reproduce the average human brain tissues characteristics at 7 T) condition, we selected three geometrical configurations with variable length that may be useful for specific human head applications.

Finally, one optimized 4R birdcage coil prototype was built. The layout was designed using Eagle software and the flexible printed-circuit-board (PCB) prototype printed on a Kapton 50-micron-thick substrate. A dedicated mechanical support for the RF coil was designed in Autocad and 3D printed using acrylonitrile butadiene styrene (ABS) plastic material. The other materials used in the design are non-magnetic chip capacitors (ATC 100C from American Technical Ceramics, RICHARDSON RFPD, Milano, Italy), RG-58 cables (Belden, RS Components Ltd., Corby, UK) and a metallic mesh (200 holes per linear inch—004 mm wire—0.077 mm aperture) arranged on the external tubes to shield the coil. The coil was characterized on the workbench measuring the S_{ii} parameters with a vector network analyzer (VNA, E5080A Agilent Technologies, Microlease S.r.l., Milano, Italy) and the coil Q factor as [5]:

$$Q = \frac{f_0}{\Delta f_{-3dB}} \quad (4)$$

at the two working frequencies. The workbench test was performed both for the empty RF coil and when loaded with a spherical phantom consistent with the one used for the numerical simulations.

3. Results

3.1. 4R Birdcage Model Optimization

Since the final target of the current study is the realization of a DT-RF birdcage coil prototype for human head imaging, the 4R coil diameter was fixed to 240 mm considering the average diameter of the human head (Figure 2). Instead, the studied three 4R birdcage-like structures require the choice of the inner and outer lengths, determining the total length. Thus, full-wave simulations based on Maxwell equations were performed to study the DT-RF coil behavior, by varying the coil length (see Figures 3–5). We started tuning each geometrical configuration of the DT-RF 4R birdcage coil model with different lengths at the two frequencies of interest with the coil without loading sample (in air). To this purpose, we have considered the following three conditions: (i) inner ^{23}Na birdcage gap between end rings (gap_{ER}) variable, having the inner ^{23}Na birdcage legs length (l_{Na}) fixed (Figure 3); (ii) inner ^{23}Na birdcage legs length (l_{Na}) variable, taking the gap between end rings (gap_{ER}) fixed (Figure 4); (iii) inner ^{23}Na birdcage legs length (l_{Na}) variable, taking the total coil length (l_{coil}) fixed (Figure 5).

DT-RF Coil starting parameters	
r_{coil}	120 mm
l_{Na}	160 mm
l_{H}	208 mm
l_{coil}	232 mm
w_{ER}	12 mm
w_{LEGS}	12 mm
r_{shield}	150 mm
l_{shield}	300 mm
gap_{ER}	12 mm

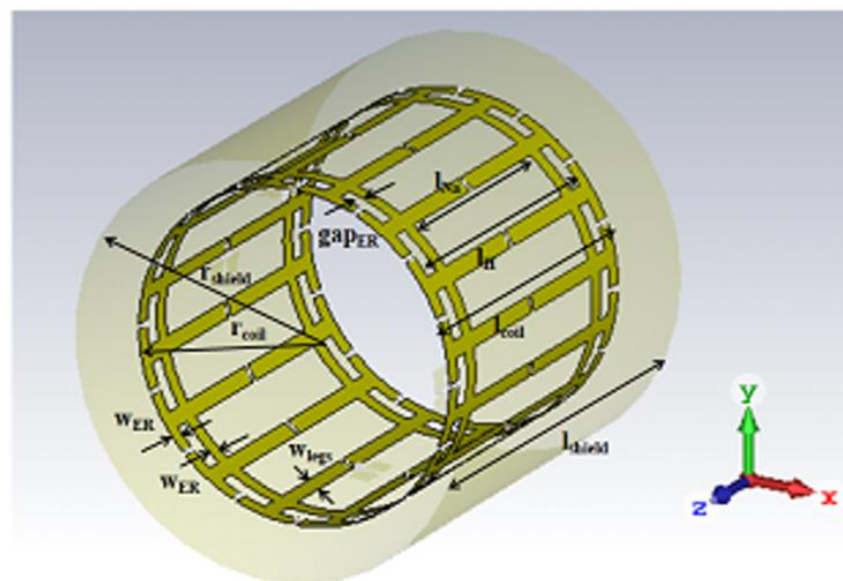


Figure 2. EM CAD model and starting dimensions of the four-ring DT-RF birdcage coil with sixteen legs.

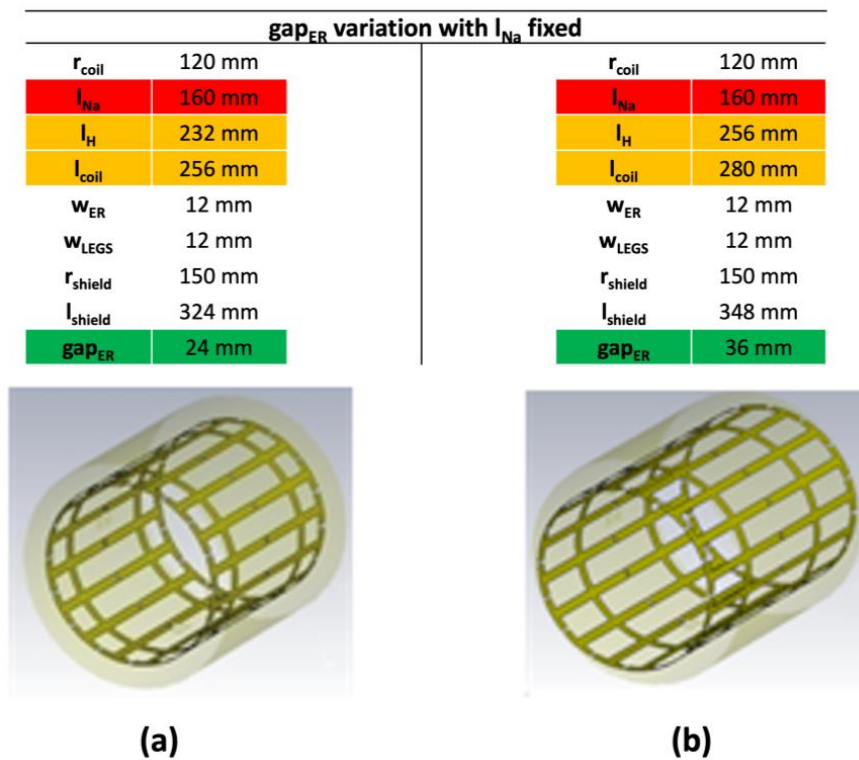


Figure 3. EM CAD model of the four-ring DT-RF coil model versus the geometrical dimensions. The gap_{ER} variable parameter is in green, while the parameters changing with the gap_{ER} parameter are in orange. In red are the fixed parameters.

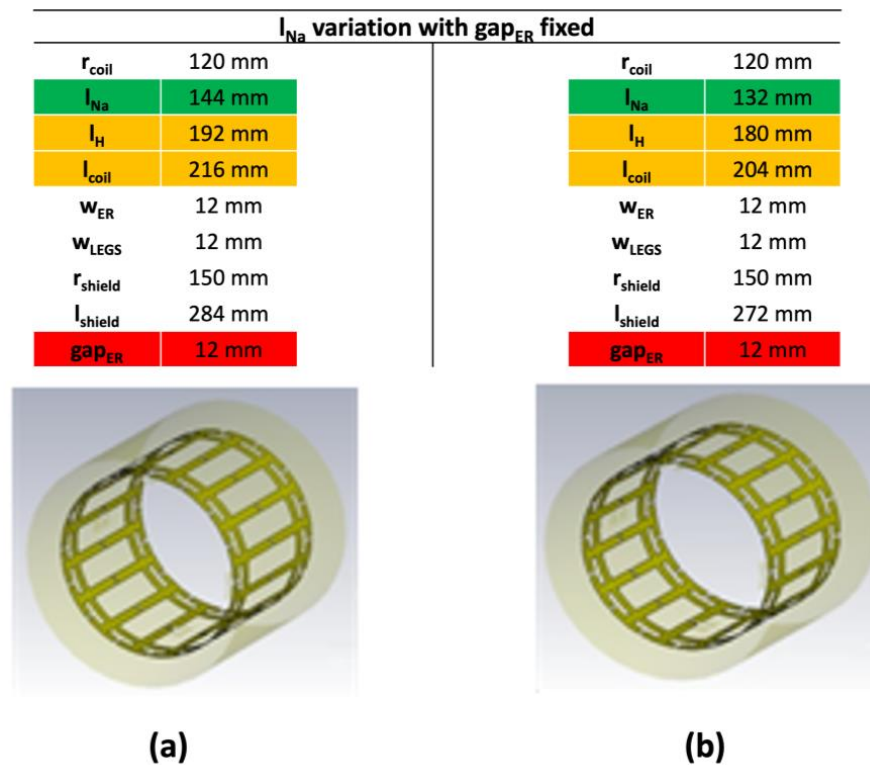


Figure 4. EM CAD model of the four-ring DT-RF coil model versus the geometrical dimensions. The I_{Na} variable parameter is in green, while the parameters changing with the I_{Na} parameter are in orange (I_H and I_{coil}). In red are the fixed parameters (gap_{ER}).

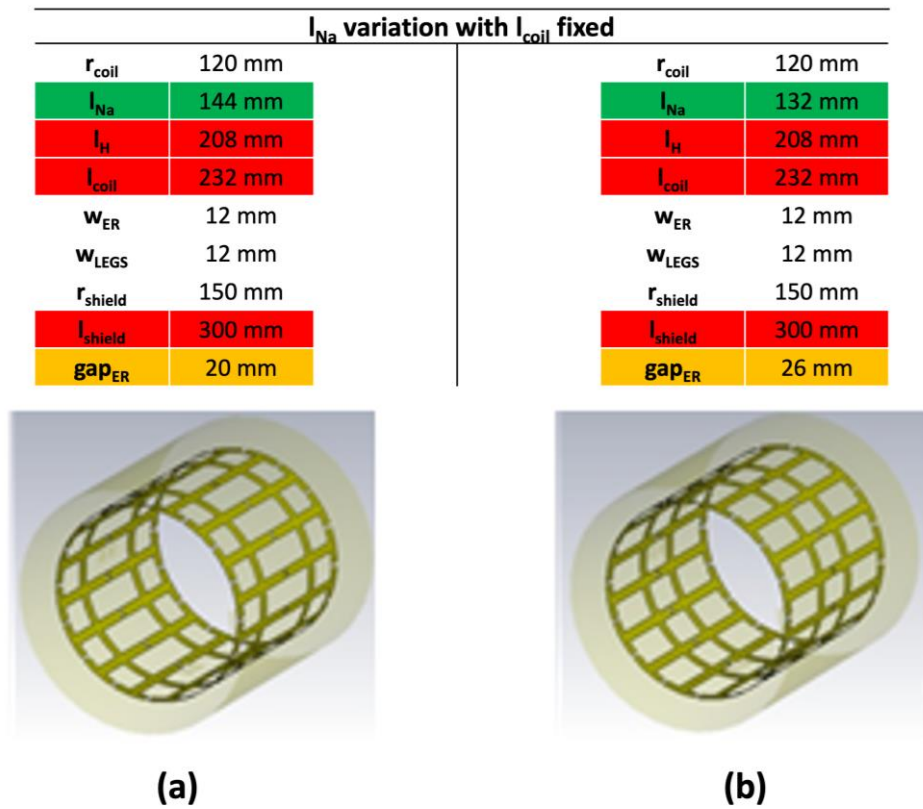


Figure 5. EM CAD model of the four-ring DT-RF coil model versus the geometrical dimensions. The I_{Na} variable parameter is in green, while the parameters changing with the I_{Na} parameter are in orange (gap_{ER}). In red are the fixed parameters (I_H , I_{coil} , I_{shield}).

Then, a cylindrical phantom model was included in the simulation models (Figure 6).

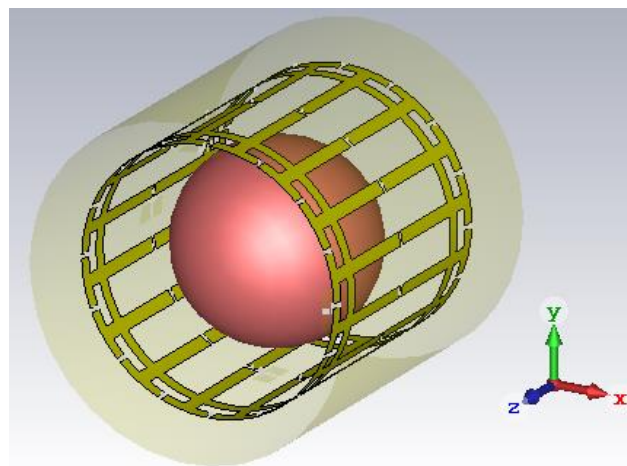


Figure 6. EM CAD model of the four-ring DT-RF coil model with the spherical phantom positioned at the center.

We performed full-wave simulations of all the above configurations and the B_1^+ field maps were extracted. From those maps we calculated the RF field homogeneity at the ^{23}Na and 1H Larmor frequencies (f_{1H} and f_{23Na}) on the transverse ($z = 0$) plane (Table 1) using Equation (2).

Table 1. $|B_1^+|$ field homogeneity calculated on the transverse plane ($z = 0$) using Equation (2).

$ B_1^+ $ Homogeneity (%)			
$l_{Na} = 160$ mm (Figure 3)			
gap _{PER} = 24 mm		gap _{PER} = 36 mm	
@ f_{1H}	44	@ f_{1H}	50
@ f_{23Na}	97	@ f_{23Na}	97
gap _{PER} = 12 mm (Figure 4)			
$l_{Na} = 144$ mm		$l_{Na} = 132$ mm	
@ f_{1H}	36	@ f_{1H}	32
@ f_{23Na}	97	@ f_{23Na}	97
$l_{coil} = 232$ mm (Figure 5)			
$l_{Na} = 144$ mm		$l_{Na} = 132$ mm	
@ f_{1H}	38	@ f_{1H}	45
@ f_{23Na}	97	@ f_{23Na}	96

To give a closer look on the spatial RF field homogeneity in the following we will concentrate on the comparison among three geometrical configurations, named accordingly to the length of the proton birdcage l_H as: long ($l_H = 256$ mm, Figure 3b), short ($l_H = 180$ mm, Figure 4b), and intermediate ($l_H = 208$ mm, Figure 5b). The normalized transverse $|B_1^+|$ field maps on the central plane ($z = 0$) of these configurations are reported in Figure 7 for the ^{23}Na and 1H Larmor frequencies. Figures 8 and 9 show, respectively, the $|B_1^+|$ profiles along the x -axis and z -axis for the three considered geometrical configurations.

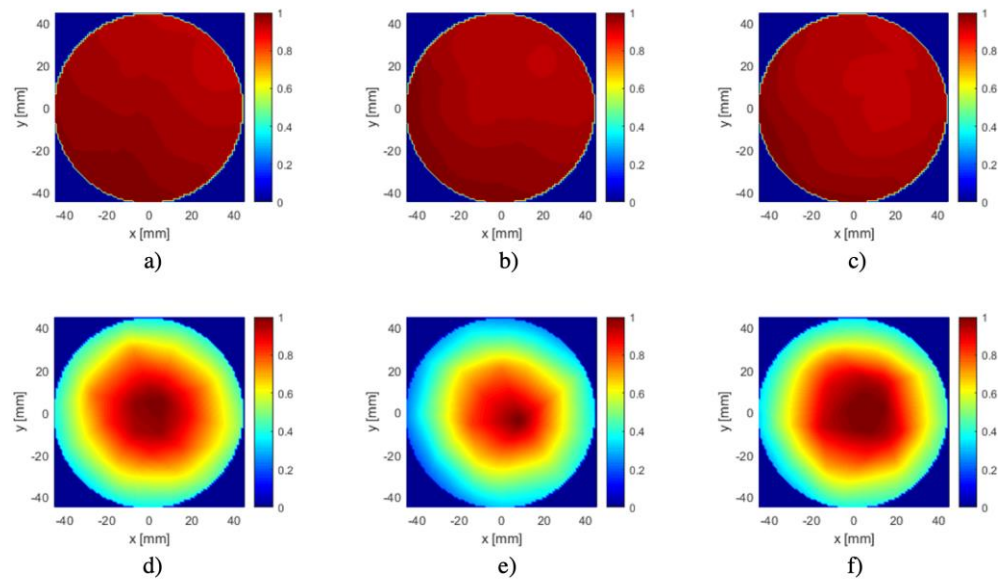


Figure 7. Normalized transverse $|B_1^+|$ field maps of the four-ring DT-RF coil model on the central plane ($z = 0$). In (a–c) for the 7 T sodium Larmor frequency of the ‘long’, ‘short’ and ‘intermediate’ configuration, respectively. In (d–f) as for the first row but for the 7 T proton Larmor frequency.

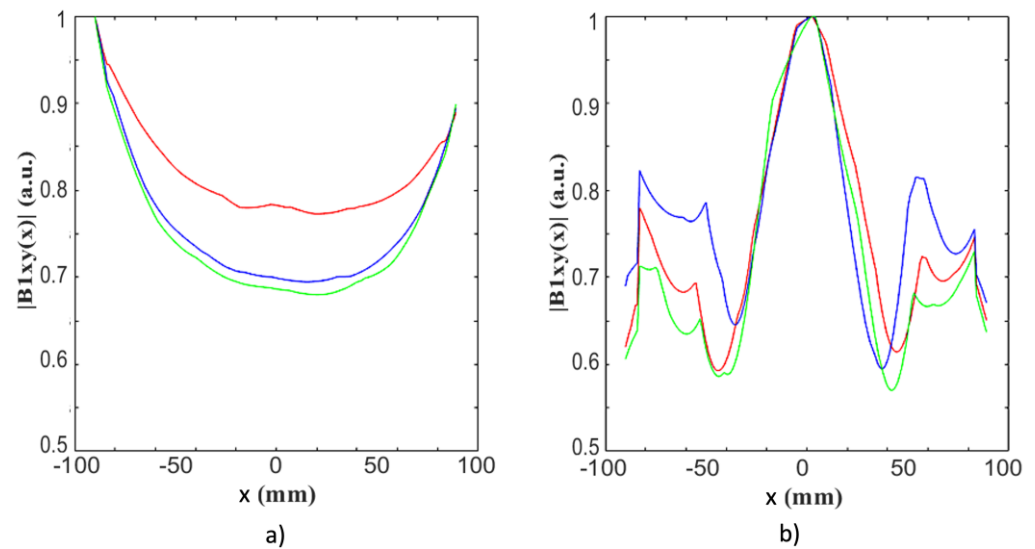


Figure 8. Transverse $|B_1^+|$ profiles along the x -axis at the sodium (a), and proton (b), Larmor frequency of the 7 T four-ring DT-RF coil model for the ‘long’ (red line), ‘short’ (blue line) and ‘intermediate’ (green line) configurations.

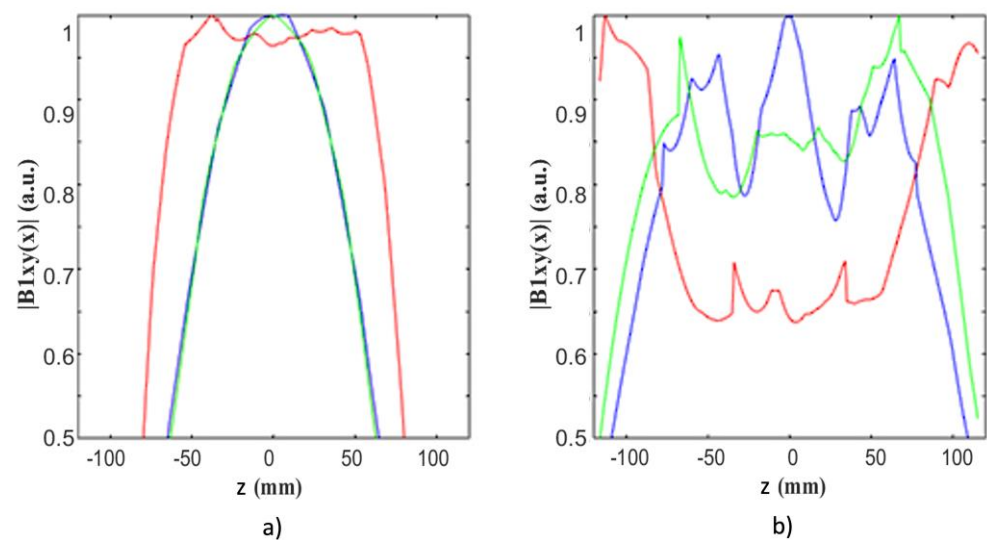


Figure 9. Longitudinal $|B_1^+|$ profiles along the z -axis at the sodium (a), and proton (b), Larmor frequency of the 7 T four-ring DT-RF coil model for the ‘long’ (red line), ‘short’ (blue line) and ‘intermediate’ (green line) configurations.

Thereafter, all geometrical configurations were matched at the two frequencies of interest and the resulting diagonal elements of the scatter matrix calculated (Table 2). With reflection coefficients always smaller than -14 dB, we proceeded with the evaluation of the RF efficiencies (Table 3) as defined in Equation (3).

3.2. The Four-Ring DT-RF Coil Prototype Workbench Testing

Taking into account the target application, the ‘intermediate’ configuration was chosen, built and tested on the workbench (Figure 10). Indeed, if the RF coil prototype is too long, the desired positioning of the patient’s head at the coil center could be problematic. The previous limitation holds for the human head imaging, but it may become irrelevant for other clinical applications (e.g., limbs).

Table 2. Simulated scattering parameters (S_{ii}) of the four-ring DT-RF coil models after matching. Port 1 refers to the first proton port; the reflection coefficient of the second proton port, S_{22} , is equal to S_{11} . Port 3 refers to the first sodium port; the reflection coefficient of the second sodium port, S_{44} , is equal to S_{33} .

S_{ii} Parameters (dB) after Matching			
$l_{Na} = 160$ mm (Figure 3)			
gap _{PER} = 24 mm		gap _{PER} = 36 mm	
$S_{11} (f_{1H})$	−27	$S_{11} (f_{1H})$	−22
$S_{33} (f_{23Na})$	−23.8	$S_{33} (f_{23Na})$	−30
$gap_{PER} = 12$ mm (Figure 4)			
$l_{Na} = 144$ mm		$l_{Na} = 132$ mm	
$S_{11} (f_{1H})$	−17	$S_{11} (f_{1H})$	−16
$S_{33} (f_{23Na})$	−29	$S_{33} (f_{23Na})$	−32
$l_{coil} = 232$ mm (Figure 5)			
$l_{Na} = 144$ mm		$l_{Na} = 132$ mm	
$S_{11} (f_{1H})$	−14	$S_{11} (f_{1H})$	−18
$S_{33} (f_{23Na})$	−32	$S_{33} (f_{23Na})$	−32

Table 3. Efficiency of the four-ring DT-RF coil models.

Efficiency ($\mu T/\sqrt{W}$)			
$l_{Na} = 160$ mm (Figure 3)			
gap _{PER} = 24 mm		gap _{PER} = 36 mm	
@ f_{1H}	1.8	@ f_{1H}	1.8
@ f_{23Na}	3.0	@ f_{23Na}	3.0
$gap_{PER} = 12$ mm (Figure 4)			
$l_{Na} = 144$ mm		$l_{Na} = 132$ mm	
@ f_{1H}	1.5	@ f_{1H}	1.7
@ f_{23Na}	3.0	@ f_{23Na}	2.9
$l_{coil} = 232$ mm (Figure 5)			
$l_{Na} = 144$ mm		$l_{Na} = 132$ mm	
@ f_{1H}	1.6	@ f_{1H}	1.7
@ f_{23Na}	2.9	@ f_{23Na}	2.9



Figure 10. The four-ring DT-RF prototype view after removing the external case (left). Detail of the coil structure with two of the four rings visible (right).

The prototype construction started by independently tuning the inner LP birdcage at the sodium Larmor frequency and the two outer birdcage-like structures at the proton Larmor frequency. The full spectra of the inner and outer structures were measured with a pick-up loop connected to the VNA and placed close to the corresponding resonating structures. Each outer birdcage-like structure behaves as a standard HP birdcage in the absence of capacitors inserted on the inner and the opposite outer structures (Figure 11). When the second birdcage-like structure is added by soldering the proper tuning capacitors, a small increase (less than 3 MHz) in the resonant frequencies was observed (Figure 12). It was likely due to a residual small inductive coupling between the two structures [41].

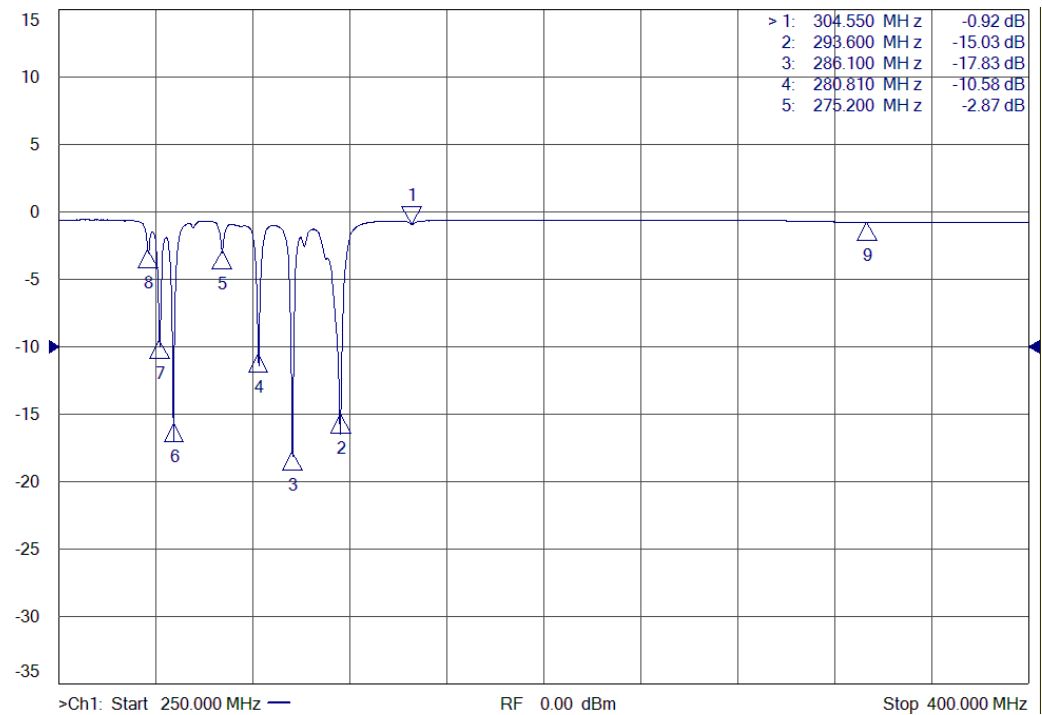


Figure 11. Full spectrum of a single outer birdcage-like structure in absence of capacitors on the inner and opposing outer structures (frequency sweep for 250 to 400 MHz).

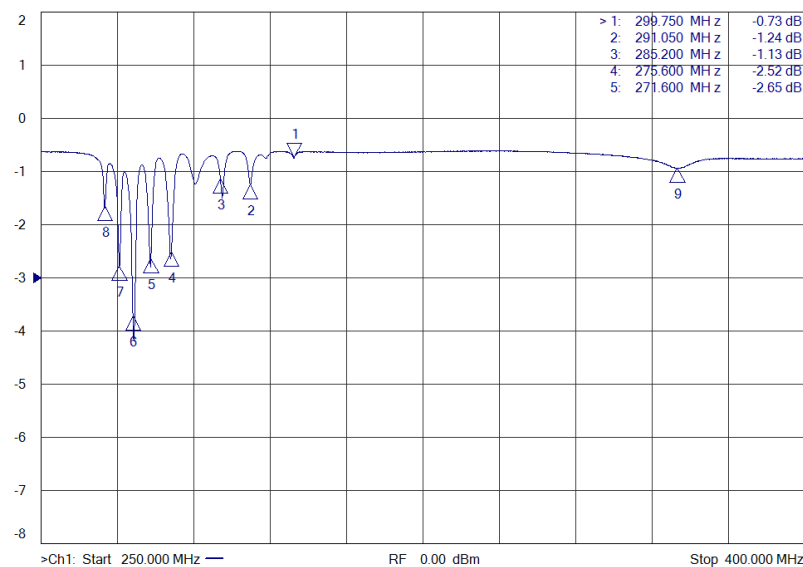


Figure 12. Full spectrum of the two outer birdcage-like structures in absence of capacitors on the inner structure (frequency sweep for 250 to 400 MHz).

After independently tuning each resonant structure at the appropriate frequency (sodium for the inner birdcage, proton for the outer ones), all the tuning capacitors (for inner and outer birdcages) were soldered again. A minor detuning was observed and adjusted. The full spectrum of the complete 4R-DT birdcage is reported in Figure 13. The homogeneous mode of the inner LP birdcage was identified as the resonance at the lowest observed frequency in the measured spectrum (marker 1 in Figure 13).

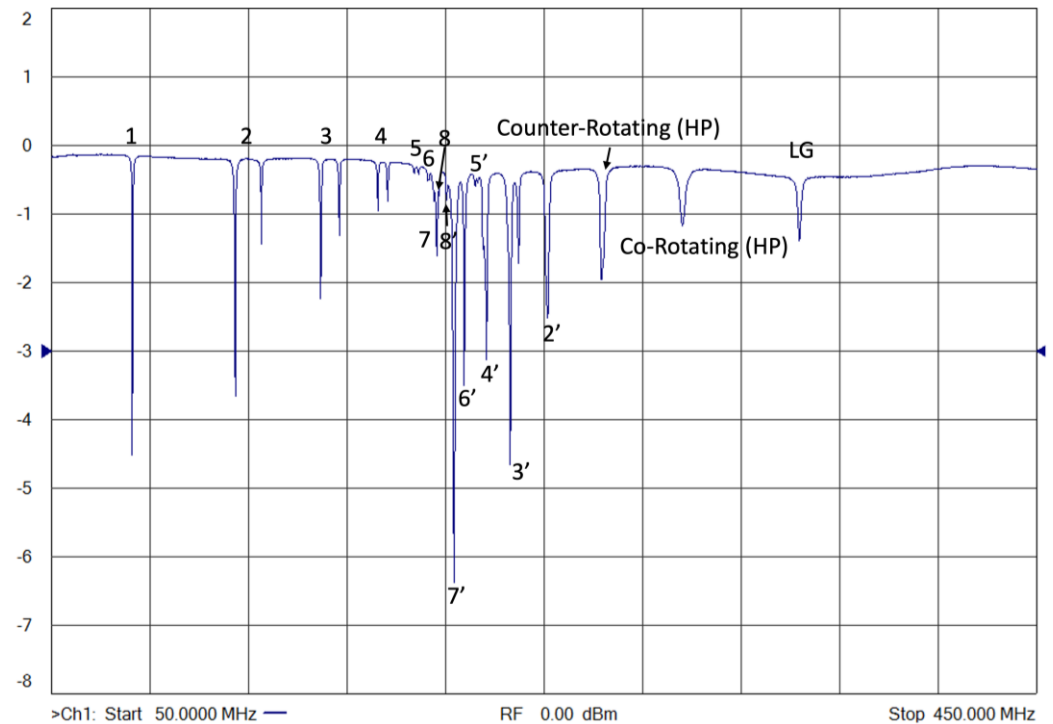


Figure 13. Measured S_{11} full spectrum of the four-ring DT-RF coil prototype with both sodium and proton resonant structures connected, frequency sweep from 50 to 450 MHz. Numbers without apex refer to the LF resonant modes (1 to 8) with frequencies 81.8, 130.4, 162.1, 184.6, 197.7, 203.3, 205.1, 207.0 MHz. Numbers with apex refer to the HF resonant modes ($8'$ to $2'$) with frequencies: 209.8, 213.6, 217.3, 222.0, 226.6, 237.9, 250.9 MHz. Counter-Rotating and co-rotating HP modes have frequencies of 273.4 and 306.1 MHz, respectively, and the LG label refers to the end-rings mode of the HP structures, which generates a longitudinal magnetic field.

Then, a cylindrical phantom model was included. The load consists of a phantom filled with a 0.05 M saline solution with the same dimensions (diameter = 180 mm) and electrical characteristics ($\sigma = 0.6$ S/m, $\epsilon_r = 80$) used for the load included in the electromagnetic model of the DT-RF coils. The Q factor at both working frequencies was measured (Table 4) both in absence (Q_{unloaded}) and in presence (Q_{loaded}) of a spherical phantom.

Table 4. Q factors of the four-ring model measured at the sodium and proton Larmor frequencies at 7 T in the unloaded and loaded conditions.

Unloaded	$Q_{\text{unloaded}} (f_{23\text{Na}})$	387
	$Q_{\text{unloaded}} (f_{1\text{H}})$	337
Loaded	$Q_{\text{loaded}} (f_{23\text{Na}})$	181
	$Q_{\text{loaded}} (f_{1\text{H}})$	172

Finally, the prototype was matched in the presence of the spherical phantom using series capacitive matching networks. The workbench measurements of the S parameters are reported in Table 5.

Table 5. Measured S_{ii} parameters of the ‘four-rings’ DT-RF coil prototype.

S_{ii} Parameters (dB)	
$S_{11} (f_{1H})$	−24
$S_{22} (f_{1H})$	−20
$S_{21} (f_{1H}) = S_{12} (f_{1H})$	−15
$S_{33} (f_{23Na})$	−14
$S_{44} (f_{23Na})$	−16
$S_{43} (f_{23Na}) = S_{34} (f_{23Na})$	−16

4. Discussion

By numerical simulations, we have shown that all the considered geometrical configurations can be successfully tuned and matched. The comparison among the models selected based on the proton resonant structure length shows that the B_1^+ field homogeneity at the proton frequency for the ‘long’ configuration is 18% higher than the ‘short’ one while the B_1^+ field homogeneity at the sodium frequency does not show a significant variation. We put emphasis on this result because at UHF-MRI the field distribution at proton frequency is a critical factor, related to the length matching among the effective electromagnetic wavelength and the sample’s dimension. Indeed, the proton frequency wavelength ($\lambda_0 \approx 1$ m in the free space at about 300 MHz) becomes $\lambda \approx 0.11$ m when the cylindrical phantom (with $\epsilon_r = 80$) is present. We also note that the improvement of the field homogeneity in the longitudinal plane at the sodium frequency, obtained by increasing the total length of the DT-RF coil, is clearly visible when comparing the ‘long’ and ‘short’ z-profiles (see Figure 9a).

From the inspection of data in Table 3, we observe how the four-ring DT-RF coil efficiency does not change significantly varying the geometrical parameters. This is an indication that, for this type of coils, the design can be optimized in terms of the desired homogeneity at the two resonant frequencies (with the constraints related to the target body district), with limited trade-off in terms of coil efficiency. The latter is instead highly dependent on the coil-to-shield ratio [6], a parameter we did not consider in this study.

In our prototype, during workbench tests, we noticed how when all the resonant structures are joint together, the two outer birdcage-like structures become strongly coupled through the inner legs and a splitting of the proton homogenous mode in a co-rotating and counter-rotating mode is observable (Figure 13). For the counter-rotating mode, no net current flows in the legs. Instead, for the co-rotating mode, the flowing RF currents generate the desired transverse magnetic field, and this is the mode useful for imaging [14]. We also demonstrated that the 4R-DT coil can be efficiently tuned and matched with return losses that, as from simulations (Table 2) and workbench tests (Table 5), are compatible with a practical implementation.

To the best of our knowledge there are no other 4R-DT coils for human head at 7 T to compare with. As previously discussed, the coil realization is relatively simple, and the main limitation of this approach is related to the increased total length of the resonant structure (when compared with the alternatively tuned legs or the concentric birdcages). This issue could be mitigated by the folded approach developed in [15] for preclinical applications but its applicability to the human head has not been demonstrated yet.

A qualitative comparison with the other two approaches is worthwhile. The alternated leg design has two main limitations: (i) because of the inductor tolerances, it is very hard to achieve $N/2$ trap circuits accurately tuned at the same frequency, and the birdcage symmetry is perturbed, with degraded magnetic field homogeneity; (ii) the insertion of $N/2$ trap circuits significantly degrades the birdcage Quality factor (Q) and the image SNR. We can also state that its construction is complex and, considering the large number of discrete components, the tuning/matching procedure can be very time-consuming. The concentric birdcages approach is attractive but, even with the optimal geometrical

orientation of the legs of the two resonators [5,6], end-rings coupling is an issue. It can be reduced, increasing the length mismatch among the two resonators [6] with the drawback of an increased total length. In this respect, it shares this disadvantage with the 4R approach but with the extra cost of a more time-consuming tuning/matching procedure.

5. Conclusions

In this study, suitable design criteria to optimize four-ring DT-RF coil designs have been reported. The design procedure has been applied to a family of numerical 4R DT-RF coil models for proton and sodium MRI of the human head at 7 T. These models have been numerically characterized considering B_1^+ field homogeneity and coil efficiency. The simulations showed how good performances, in terms of both parameters, can be achieved for human head imaging, with a careful optimization of the design parameters. A close to optimal configuration was manufactured and tested on the workbench. The experimental test was useful to define the tuning and matching procedure, verify the resonance spectrum and check the achievable conditions in terms of scattering parameters.

In conclusion, the final geometrical parameters of the 4R DT-RF coil model and prototype were selected considering the final target of MRI imaging of the human head at 7 T. We anticipate that other geometrical conditions could be selected to allow a wider class of clinical applications at 7 T with the 4R DT-RF coil design.

Author Contributions: Conceptualization, F.M., A.R. and M.A.; methodology, F.M., A.R., G.G., E.B., F.R., M.T., G.T., M.F., M.A. and A.G.; software, F.M. and A.G.; validation, F.M., A.R., G.G., E.B., F.R., M.T., G.T., M.F., M.A. and A.G.; formal analysis, F.M.; investigation, F.M., A.R., M.A. and A.G.; resources, A.R. and M.T.; data curation, F.M.; writing—original draft preparation, F.M. and A.R.; writing—review and editing, A.R., G.G., M.A. and A.G.; visualization, F.M.; supervision, A.R., M.T. and A.G.; project administration, A.R. and M.A.; funding acquisition, A.R., M.T. and M.A. All authors have read and agreed to the published version of the manuscript.

Funding: This research has been partially funded by the Italian National Institute for Nuclear Physics, within the project nextMR (Advancing Magnetic Resonance Imaging and Data Analysis, INFN-CSN5).

Data Availability Statement: Not applicable.

Acknowledgments: This work has been partially supported also by the Italian Ministry of Health under the grant RC-Linea4 and “5 per mille” to IRCCS Fondazione Stella Maris.

Conflicts of Interest: The authors declare no conflict of interest.

References

1. Hayes, C.E.; Edelstein, W.A.; Schenck, J.F.; Mueller, O.M.; Eash, M. An efficient, highly homogeneous radiofrequency coil for whole-body NMR imaging at 1.5 T. *J. Magn. Reson.* **1985**, *63*, 622–628. [[CrossRef](#)]
2. Tropp, J. The theory of the bird-cage resonator. *J. Magn. Reson.* **1989**, *82*, 51–62. [[CrossRef](#)]
3. Leifer, M.C. Resonant Modes of the Birdcage Coil. *J. Magn. Reson.* **1997**, *124*, 51–60. [[CrossRef](#)]
4. Tropp, J. Mutual inductance in the bird-cage resonator. *J. Magn. Reson.* **1997**, *126*, 9–17. [[CrossRef](#)] [[PubMed](#)]
5. Mispelter, J.; Lupu, M.; Briguët, A. *NMR Probeheads for Biophysical and Biomedical Experiments: Theoretical Principles & Practical Guidelines*, 2nd ed.; Imperial College Press: London, UK, 2015.
6. Fantasia, M.; Galante, A.; Maggiorelli, F.; Retico, A.; Fontana, N.; Monorchio, A.; Alecci, M. Numerical and workbench design of 2.35 T double-tuned ($^1\text{H}/^{23}\text{Na}$) nested RF birdcage coils suitable for animal size MRI. *IEEE Trans. Med. Imaging* **2020**, *39*, 3175–3186. [[CrossRef](#)]
7. Isaac, G.; Schnall, M.D.; Lenkinski, R.E.; Vogeleson, K. A design for a Double-Tuned Birdcage Coil for Use in an Integrated MRI/MRS Examination. *J. Magn. Reson.* **1990**, *89*, 41–50. [[CrossRef](#)]
8. Shen, G.X.; Boada, F.E.; Thulborn, K.R. Dual-frequency, dual-quadrature, birdcage RF coil design with identical B_1 pattern for sodium and proton imaging of the human brain at 1.5 T. *Magn. Reson. Med.* **1997**, *38*, 717–725. [[CrossRef](#)] [[PubMed](#)]
9. Matson, G.B.; Vermathen, P.; Hill, T.C. A practical double-tuned $^1\text{H}/^{31}\text{P}$ quadrature birdcage headcoil optimized for ^{31}P operation. *Magn. Reson. Med.* **1999**, *42*, 173. [[CrossRef](#)]
10. Giovannetti, G.; Valvano, G.; Virgili, G.; Giannoni, M.; Flori, A.; Frijia, F.; De Marchi, D.; Hartwig, V.; Landini, L.; Aquaro, G.D.; et al. Design and simulation of a dual-tuned $^1\text{H}/^{23}\text{Na}$ birdcage coil for MRS studies in human calf. *Appl. Magn. Reson.* **2015**, *46*, 1221–1238. [[CrossRef](#)]
11. Fitzsimmons, J.R.; Beck, B.L.; Brooker, H.R. Double resonant quadrature birdcage. *Magn. Reson. Med.* **1993**, *30*, 107–114. [[CrossRef](#)] [[PubMed](#)]

12. Asfour, A. A three-coil RF probe-head at 2.35 T: Potential applications to the ^{23}Na and to the hyperpolarized ^{129}Xe MRI in small animals. In Proceedings of the 2010 Annual International Conference of the IEEE Engineering in Medicine and Biology, Buenos Aires, Argentina, 31 August–4 September 2010; pp. 5693–5699. [[CrossRef](#)]
13. Brand, R.C.; Webb, A.G.; Beenakker, J.M. Design and Performance of a Transformer-Coupled Double Resonant Quadrature Birdcage Coil for Localized Proton and Phosphorus Spectroscopy in the Human Calf Muscle. *Conc. Magn. Reson.* **2013**, *42*, 155–164. [[CrossRef](#)]
14. Murphy-Boesch, J.; Srinivasan, R.; Carvajal, L.; Brown, R.R. Two configurations of the four-ring birdcage coil for ^1H imaging and ^1H decoupled ^{31}P spectroscopy of the human head. *J. Magn. Reson.* **1994**, *B103*, 103–114. [[CrossRef](#)] [[PubMed](#)]
15. Ha, Y.; Choi, C.H.; Worthoff, W.A.; Shymanskaya, A.; Schöneck, M.; Willuweit, A.; Felder, J.; Shah, N.J. Design and use of a folded four-ring double-tuned birdcage coil for rat brain sodium imaging at 9.4 T. *J. Magn. Reson.* **2018**, *286*, 110–114. [[CrossRef](#)] [[PubMed](#)]
16. Lanz, T.; von Kienlin, M.; Behr, W.; Haase, A. Double-tuned four-ring birdcage resonators for in vivo ^{31}P -nuclear magnetic resonance spectroscopy at 11.75 T. *Magn. Reson. Mat. Phys. Biol. Med.* **1997**, *5*, 243–246. [[CrossRef](#)]
17. Wiggins, G.C.; Brown, R.; Lakshmanan, K. High-performance radiofrequency coils for ^{23}Na MRI: Brain and musculoskeletal applications. *NMR Biomed.* **2016**, *29*, 96–106. [[CrossRef](#)] [[PubMed](#)]
18. Murphy-Boesch, J. Double-tuned birdcage coils: Construction and tuning. In *eMagRes*; Harris, R.K., Wasylshen, R.L., Eds.; John Wiley & Sons: Hoboken, NJ, USA, 2011. [[CrossRef](#)]
19. Shan, K.; Duan, Y. Rapid four-ring birdcage coil analysis: Design optimization for high efficiency, low interference, and improved body loading tolerance. *Magn. Reson. Imag.* **2019**, *66*, 30–35. [[CrossRef](#)] [[PubMed](#)]
20. Hong, S.M.; Choi, C.H.; Shah, N.J.; Felder, J. Design and evaluation of a $^1\text{H}/^{31}\text{P}$ double-resonant helmet coil for 3T MRI of the brain. *Phys. Med. Biol.* **2019**, *64*, 035003. [[CrossRef](#)] [[PubMed](#)]
21. Findekle, C.; Leussler, C.; Morich, M.; Demeester, G. Efficient Design of a novel Double Tuned Quadrature Headcoil for Simultaneous ^1H and ^{31}P MRI/MRS at 7T. *Proc. Intl. Soc. Mag. Reson. Med.* **2005**, *13*, 891.
22. Hilal, S.K.; Maudsley, A.A.; Simon, H.E.; Perman, W.H.; Bonn, J.; Mawad, M.E.; Silver, A.J.; Ganti, S.R.; Sane, P.; Chien, I.C. In vivo NMR imaging of tissue sodium in the intact cat before and after acute cerebral stroke. *Am. J. Neuroradiol.* **1983**, *4*, 245–249.
23. Boada, F.E.; LaVerde, G.; Jungreis, C.; Nemoto, E.; Tanase, C.; Hancu, F. Loss of cell ion homeostasis and cell viability in the brain: What sodium MRI can tell us. *Curr. Top. Dev. Biol.* **2005**, *70*, 77–101. [[CrossRef](#)] [[PubMed](#)]
24. Thulborn, K.R.; Gindin, T.S.; Davis, D.; Erb, P. Comprehensive MR imaging protocol for stroke management: Tissue sodium concentration as a measure of tissue viability in nonhuman primate studies and in clinical studies. *Radiology* **1999**, *213*, 156–166. [[CrossRef](#)] [[PubMed](#)]
25. Thulborn, K.R.; Davis, D.; Snyder, J.; Yonas, H.; Kassam, A. Sodium MR imaging of acute and subacute stroke for assessment of tissue viability. *Neuroimag. Clin. N. Am.* **2005**, *15*, 639–653. [[CrossRef](#)]
26. Sandstede, J.J.W.; Hillenbrand, H.; Beer, M.; Pabst, T.; Butter, F.; Machann, W.; Bauer, W.; Hahn, D.; Neubauer, S. Time course of ^{23}Na signal intensity after myocardial infarction in humans. *Magn. Reson. Med.* **2004**, *52*, 545–551. [[CrossRef](#)] [[PubMed](#)]
27. Pabst, T.; Sandstede, J.; Beer, M.; Kenn, W.; Greiser, A.; von Kienlin, M.; Neubauer, S.; Hahn, D. Optimization of ECG-triggered 3D ^{23}Na MRI of the human heart. *Magn. Reson. Med.* **2001**, *45*, 164–166. [[CrossRef](#)] [[PubMed](#)]
28. Sandstede, J.W.; Pabst, T.; Beer, M.; Lipke, C.; Baurle, K.; Butter, F.; Harre, K.; Kenn, W.; Voelker, W.; Neubauer, S.; et al. Assessment of myocardial infarction in humans with ^{23}Na MR imaging: Comparison with cine MR imaging and delayed contrast enhancement. *Radiology* **2001**, *221*, 222–228. [[CrossRef](#)] [[PubMed](#)]
29. Maril, N.; Rosen, Y.; Reynolds, G.H.; Ivanishev, A.; Ngo, L.; Lenkinski, R.E. Sodium MRI of the human kidney at 3 Tesla. *Magn. Reson. Med.* **2006**, *56*, 1229–1234. [[CrossRef](#)]
30. Steidle, G.; Graf, H.; Schick, F. Sodium 3-D MRI of the human torso using a volume coil. *Magn. Reson. Imag.* **2004**, *22*, 171–180. [[CrossRef](#)] [[PubMed](#)]
31. Wheaton, A.J.; Borthakur, A.; Shapiro, E.M.; Regatte, R.R.; Akella, S.V.S.; Kneeland, J.B.; Reddy, R. Proteoglycan loss in human knee cartilage: Quantitation with sodium MR imaging—Feasibility study. *Radiology* **2004**, *231*, 900–905. [[CrossRef](#)] [[PubMed](#)]
32. Insko, E.K.; Clayton, D.B.; Elliott, M.A. In vivo sodium MR imaging of the intervertebral disk at 4 T. *Acad. Radiol.* **2002**, *9*, 800–804. [[CrossRef](#)] [[PubMed](#)]
33. Weber, M.A.; Nielles-Vallespin, S.; Essig, M.; Jurkat-Rott, K.; Kauczor, H.U.; Lehmann-Horn, F. Muscle Na^+ channelopathies—MRI detects intracellular ^{23}Na accumulation during episodic weakness. *Neurology* **2006**, *67*, 1151–1158. [[CrossRef](#)] [[PubMed](#)]
34. Constantinides, C.D.; Gillen, J.S.; Boada, F.E.; Pomper, M.G.; Bottomley, P.A. Human skeletal muscle: Sodium MR imaging and quantification-potential applications in exercise and disease. *Radiology* **2000**, *216*, 559–568. [[CrossRef](#)] [[PubMed](#)]
35. Schmitt, B.; Zbyn, S.; Stelzeneder, D.; Jellus, V.; Paul, D.; Lauer, L.; Trattinig, S. Cartilage Quality Assessment by Using Glycosaminoglycan Chemical Exchange Saturation Transfer and ^{23}Na RM Imaging at 7T. *Radiology* **2011**, *260*, 257–264. [[CrossRef](#)] [[PubMed](#)]
36. Ouwerkerk, R.; Bleich, K.B.; Gillen, J.S.; Pomper, M.G.; Bottomley, P.A. Tissue sodium concentration in human brain tumors as measured with ^{23}Na MR imaging. *Radiology* **2003**, *227*, 529–537. [[CrossRef](#)]
37. Nielles-Vallespin, S.; Weber, M.A.; Bock, M.; Bongers, A.; Speier, P.; Combs, S.E.; Wohrle, J.; Lehmann-Horn, F.; Essig, M.; Schad, L.R. 3D radial projection technique with ultrashort echo times for sodium MRI: Clinical applications in human brain and skeletal muscle. *Magn. Reson. Med.* **2007**, *57*, 74–81. [[CrossRef](#)] [[PubMed](#)]

38. Hoult, D.; Chen, C.; Sank, V. Quadrature detection in the laboratory frame. *Magn. Reson. Med.* **1984**, *1*, 339–353. [[CrossRef](#)] [[PubMed](#)]
39. Stara, R.; Fontana, N.; Tiberi, G.; Monorchio, A.; Manara, G.; Alfonsetti, M.; Galante, A.; Vitacolonna, A.; Alecci, M.; Retico, A.; et al. Validation of numerical approaches for electromagnetic characterization of magnetic-resonance radio-frequency coils. *Prog. Electromagn. Res. M* **2013**, *29*, 121–136. [[CrossRef](#)]
40. MS 3-2008 R2014; Determination of Image Uniformity in Diagnostic Magnetic Resonance Images. National Electrical Manufacturers Association NEMA Standards Publication: Rosslyn, VA, USA, 2021.
41. Tropp, J. The theory of an arbitrarily perturbed birdcage resonator and a Simple Method for Restoring It to Full Symmetry. *J. Magn. Reson.* **1991**, *95*, 235–243. [[CrossRef](#)]

Disclaimer/Publisher’s Note: The statements, opinions and data contained in all publications are solely those of the individual author(s) and contributor(s) and not of MDPI and/or the editor(s). MDPI and/or the editor(s) disclaim responsibility for any injury to people or property resulting from any ideas, methods, instructions or products referred to in the content.